


# RadioAstron reveals a spine-sheath jet structure in 3C 273

G. Bruni<sup>1</sup> , J. L. Gómez<sup>2</sup>, L. Vega-García<sup>3</sup>, A. P. Lobanov<sup>3,7</sup>, A. Fuentes<sup>2</sup>, T. Savolainen<sup>4,5,3</sup>, Y. Y. Kovalev<sup>6,7,3</sup>, M. Perucho<sup>8,9</sup>, J.-M. Martí<sup>8,9</sup>, J. M. Anderson<sup>10,11</sup>, P. G. Edwards<sup>12</sup>, L. I. Gurvits<sup>13,14,12</sup>, M. M. Lisakov<sup>3,6</sup>, A. B. Pushkarev<sup>15,6</sup>, K. V. Sokolovsky<sup>16,17</sup>, and J. A. Zensus<sup>3</sup>

<sup>1</sup> INAF – Istituto di Astrofisica e Planetologia Spaziali, Via del Fosso del Cavaliere, 100, 00133 Rome, Italy  
 e-mail: [gabriele.bruni@inaf.it](mailto:gabriele.bruni@inaf.it)

<sup>2</sup> IAA – Instituto de Astrofísica de Andalucía-CSIC, Glorieta de la Astronomía s/n, 18008 Granada, Spain

<sup>3</sup> MPIfR – Max Planck Institute for Radio Astronomy, Auf dem Hügel, 69, 53121 Bonn, Germany

<sup>4</sup> Aalto University Metsähovi Radio Observatory, Metsähovintie 114, 02540 Kylmälä, Finland

<sup>5</sup> Aalto University Department of Electronics and Nanoengineering, PL 15500, 00076 Aalto, Finland

<sup>6</sup> Lebedev Physical Institute of the Russian Academy of Sciences, Leninsky Prospekt 53, 119991 Moscow, Russia

<sup>7</sup> Moscow Institute of Physics and Technology, Institutsky Per. 9, Dolgoprudny 141700, Moscow Region, Russia

<sup>8</sup> Departament d’Astronomia i Astrofísica, Universitat de València, C/ Dr. Moliner, 50, 46100 Burjassot, València, Spain

<sup>9</sup> Observatori Astronòmic, Universitat de València, C/ Catedràtic José Beltrán, 2, 46980 Paterna, València, Spain

<sup>10</sup> Technische Universität Berlin, Institut für Geodäsie und Geoinformationstechnik, Fakultät VI, Sekr. KAI 2-2, Kaiserin-Augusta-Allee 104-106, 10553 Berlin, Germany

<sup>11</sup> GFZ German Research Centre for Geosciences, Telegrafenberg, 14473 Potsdam, Germany

<sup>12</sup> CSIRO Astronomy and Space Science, PO Box 76, Epping, NSW 1710, Australia

<sup>13</sup> JIVE – Joint Institute for VLBI ERIC, Oude Hoogeveensedijk 4, 7991 PD Dwingekoo, The Netherlands

<sup>14</sup> Dept. of Astrodynamics and Space Missions, Delft University of Technology, Kluyverweg 1, 2629 HS Delft, The Netherlands

<sup>15</sup> Crimean Astrophysical Observatory, Nauchny 298409, Crimea, Russia

<sup>16</sup> Department of Physics and Astronomy, Michigan State University, East Lansing, Michigan 48824, USA

<sup>17</sup> Sternberg Astronomical Institute, Moscow State University, Universitetskii Pr. 13, 119992 Moscow, Russia

Received 14 September 2020 / Accepted 13 July 2021

## ABSTRACT

We present Space-VLBI RadioAstron observations at 1.6 GHz and 4.8 GHz of the flat spectrum radio quasar 3C 273, with detections on baselines up to 4.5 and 3.3 Earth Diameters, respectively. Achieving the best angular resolution at 1.6 GHz to date, we have imaged limb-brightening in the jet, not previously detected in this source. In contrast, at 4.8 GHz, we detected emission from a central stream of plasma, with a spatial distribution complementary to the limb-brightened emission, indicating an origin in the spine of the jet. While a stratification across the jet width in the flow density, internal energy, magnetic field, or bulk flow velocity are usually invoked to explain the limb-brightening, the different jet structure detected at the two frequencies probably requires a stratification in the emitting electron energy distribution. Future dedicated numerical simulations will allow the determination of which combination of physical parameters are needed to reproduce the spine-sheath structure observed by Space-VLBI with RadioAstron in 3C 273.

**Key words.** galaxies: active – galaxies: jets – quasars: individual: 3C 273

## 1. Introduction

About 10% of active galactic nuclei (AGN) have prominent relativistic jets of plasma extending up to megaparsec-scale distances from the supermassive black hole (SMBH) which powers them (see e.g. [Sikora et al. 2007](#) and references therein). These are readily studied at radio wavelengths, and propagate in the inner near-nucleus segment as an outflow with a parabolic shape switching to a nearly conical one down the stream (e.g. [Asada & Nakamura 2012](#); [Kovalev et al. 2020a](#); [Nokhrina et al. 2020](#)). The launching, acceleration, and collimation of such relativistic jets are the subjects of ongoing theoretical and observational studies. The two most accredited models are the [Blandford & Znajek \(1977\)](#) mechanism, in which the rotational energy of the black hole powers jet launching, and the [Blandford & Payne \(1982\)](#) mechanism, in which the accretion disk produces a magnetically driven wind. More recently, a spine-sheath model, involving a stratified inner

jet, has been proposed and developed by different authors (e.g. [Pelletier & Roland 1989](#); [Sol et al. 1989](#); [Celotti et al. 2001](#); [Ghisellini et al. 2005](#); [Tavecchio & Ghisellini 2008](#); [D’Arcangelo et al. 2009](#); [Xie et al. 2012](#); [Mimica et al. 2015](#)). In this scenario, the jet flow consists of two different fluids: a fast, low-density component, streaming along the central axis (spine) and emerging from the immediate vicinity of the black hole, and a slower, denser component at the edges (sheath) of the conical jet, emerging from the accretion disk. This would imply that both the [Blandford & Znajek \(1977\)](#) and the [Blandford & Payne \(1982\)](#) mechanisms can be invoked to produce the two components of the outflow ([Hardee 2007](#); [Xie et al. 2012](#)). Notably, as an effect of relativistic Doppler boosting on photons, the spine would dominate the overall jet emission in blazars (having a small viewing angles from the jet axis), while the sheath would be more evident in radio galaxies (seen at large viewing angles).

The very long baseline interferometry (VLBI) technique enables the parsec-scale structure of nearby AGN jets to be

resolved and the structure of such outflows to be studied in great detail, including the inner regions in the proximity of the jet base. This powerful technique has allowed prominent emission from the jet edges – also known as limb-brightening, and related to the sheath structure mentioned above – to be detected in a number of sources. Among the pioneering works on this topic, [Attridge et al. \(1999\)](#) presented the first linear polarization observations of a spine/sheath structure in the quasar 1055+018, performed with the very long baseline array (VLBA). Later, a similar structure in the BL Lac Mrk 501 was found by different authors: [Giroletti et al. \(2004\)](#) through observations with the first dedicated Space VLBI (SVLBI) mission, VSOP/HALCA, revealed a limb brightening in the jet structure, and explained that in terms of a velocity gradient in the jet. Moreover, [Pushkarev et al. \(2005\)](#) confirmed the result detecting a spine-sheath polarization structure with the VLBA. More recently, [Boccardi et al. \(2016\)](#) presented global millimeter VLBI array (GMVA) observations of Cygnus A at 86 GHz, revealing a limb-brightening in the jet flow, with a transverse width suggesting a launching point in the accretion disk rather than in the SMBH vicinity. [Kim et al. \(2018\)](#) stacked five GMVA epochs to image the jet base in M87, finding that the limb-brightened structure could be anchored in the inner portion of the accretion disk, similarly to Cygnus A. A stratification of the jet flow in the same source was previously found by [Mertens et al. \(2016\)](#), through the kinematic analysis of multiple VLBA images at 43 GHz. Finally, [Giovannini et al. \(2018\)](#) used Space VLBI RadioAstron observations (see below) to reveal a bright outer jet layer in 3C 84, with a wide jet base suggesting either a rapid lateral expansion of the jet within  $100 r_g$  from the black hole or an origin in the accretion disk.

The RadioAstron (hereafter RA) SVLBI mission ([Kardashev et al. 2013](#)), led by the Astro Space Center (ASC, Moscow, Russia) and the Lavochkin Scientific and Production Association (Khimki, Russia), operated between 2011 and 2019. With a diameter of 10 m, the RA space radio telescope performed interferometric observations with arrays of ground radio telescopes, with a maximum Earth-space baseline at apogee of  $\sim 350\,000$  km. It operated at 0.32 GHz (*P*-band), 1.6 GHz (*L*-band), 4.8 GHz (*C*-band), and 22 GHz (*K*-band). Three key science programmes (KSPs) on AGN imaging have collected data since 2013 to study the launching, collimation, and magnetic field properties of jets in known AGN (see [Bruni et al. 2020](#) for a summary of previous results and observed targets) while the AGN survey studied properties of their cores (e.g. [Kovalev et al. 2016, 2020b](#)). In particular, the RA AGN polarization KSP aims to probe the jet structure and magnetic fields configuration at angular resolution down to a few tens of  $\mu$ as, in AGN known to have the most prominent polarization properties. More than 20 imaging experiments have been performed. Within the project, observations at 22 GHz of BL Lac from the first observing period (Announcement of Opportunity 1, AO-1, July 2013–June 2014) were presented in [Gómez et al. \(2016\)](#), producing the image with the highest angular resolution to date (21  $\mu$ as) and revealing helical magnetic fields in the jet.

The flat-spectrum radio source 3C 273, the subject of this work, is the first identified quasar ([Hazard et al. 1963](#); [Oke 1963](#); [Schmidt 1963](#)). One of the most observed VLBI targets, 3C 273 offered an opportunity for studying the jet cross-section morphology with VSOP/HALCA ([Lobanov & Zensus 2001](#)). The quasar 3C 273 was also investigated by RA in a non-imaging mode. These observations at 18, 6 and 1.3 cm resulted in the detection of the brightness temperatures in the core of

the source exceeding the inverse Compton limit ([Kovalev et al. 2016](#)) and potential refractive substructure ([Johnson et al. 2016](#)). The source was targeted twice as a part of the RA AGN polarization KSP: [Bruni et al. \(2017\)](#) performed 22 GHz observations of 3C 273, showing a brightness temperature drop of two orders of magnitude in only one year compared to [Kovalev et al. \(2016\)](#).

Here we present a two-frequency, 1.6 and 4.8 GHz, study of the jet structure in 3C 273. Taking advantage of the unprecedented angular resolution offered by RA at 1.6 GHz, we imaged for the first time a limb-brightened jet structure for this source, with a spatial distribution complementary to a spine-dominated emission detected at 4.8 GHz during previous RA observations, performed in the framework of the Strong AGN KSP. A comparison with the 4.8 GHz RA images allows us to consider a new insight in the properties of the jet flow.

## 2. RadioAstron observations and data processing

Observations at 1.6 GHz were performed on 2014 June 13, under project code GA030F for ground antennas and raks04f for RA. The array was composed of antennas in Russia (Kalyazin 64 m, Badary 32 m, Zelenchukskaya 32 m), Japan (Usuda 64 m), Australia (ATCA  $5 \times 22$  m, Ceduna 30 m, Hobart 26 m, Mopra 22 m, Parkes 64 m), New Zealand (Warkworth 12 m) and South Africa (Hartebeesthoek 26 m). The tracking station for RA was Pushchino for the entire experiment. The total observing time was 9 h (05–14 UT). RA participated with 10 scans, 14.5 min each, for a total of 2.4 h on target, covering the space-baselines between 1.6 and 4.5 Earth diameters (ED). Observations at 4.8 GHz were performed on 2014 April 30 with the project code GL038F for the ground array and raks05d for RA. The antennas composing the ground array were in Russia (Kalyazin 64 m), Australia (Ceduna, Hobart), South Africa (Hartebeesthoek), USA (Mauna Kea 25 m), and Europe (Effelsberg 100 m, Noto 32 m, Onsala 25 m, Torun 32 m, Yebes 40 m, Westerbork  $11 \times 25$  m). The tracking station for RA was Pushchino for the entire experiment. The total observing time was 12 h (10–22 UT). RA participated with 27 scans, 9.5 min each, for a total of 4.3 h on target, covering the space-baselines between 0.9 and 3.3 ED. Figure 1 presents *uv*-coverage in the two RA experiments discussed in this work. The data from both observing bands were processed at the MPIfR correlator, making use of the RA-dedicated version of DiFX software VLBI correlator ([Bruni et al. 2016](#)). Fringe-fitting at the correlator stage was performed using the largest available antennas as references for each experiment (ATCA, Parkes, Effelsberg), first setting the clock value for the ground array antennas, and then searching for signal in each RA scan: this allowed us to have a first-order solution for each space-ground scan that could later be refined through baseline-stacking (see below for details). For scans giving no fringes, we applied extrapolated clock values from the successful part of the experiment.

The following data reduction strategy in AIPS<sup>1</sup>, proven to be successful for RA AGN imaging projects, was adopted for both experiments. First, the a priori amplitude calibration was applied using the values for the antenna gains and system temperature measured at each antenna during the observations. A parallactic angle correction was applied to the ground array antennas to account for the axis rotation of the antenna feeds with respect to the target source. The data were then fringe-fitted. The ground array data were fringe-fitted first, then the SVLBI baselines, using stacked solutions of the ground

<sup>1</sup> <http://www.aips.nrao.edu/index.shtml>

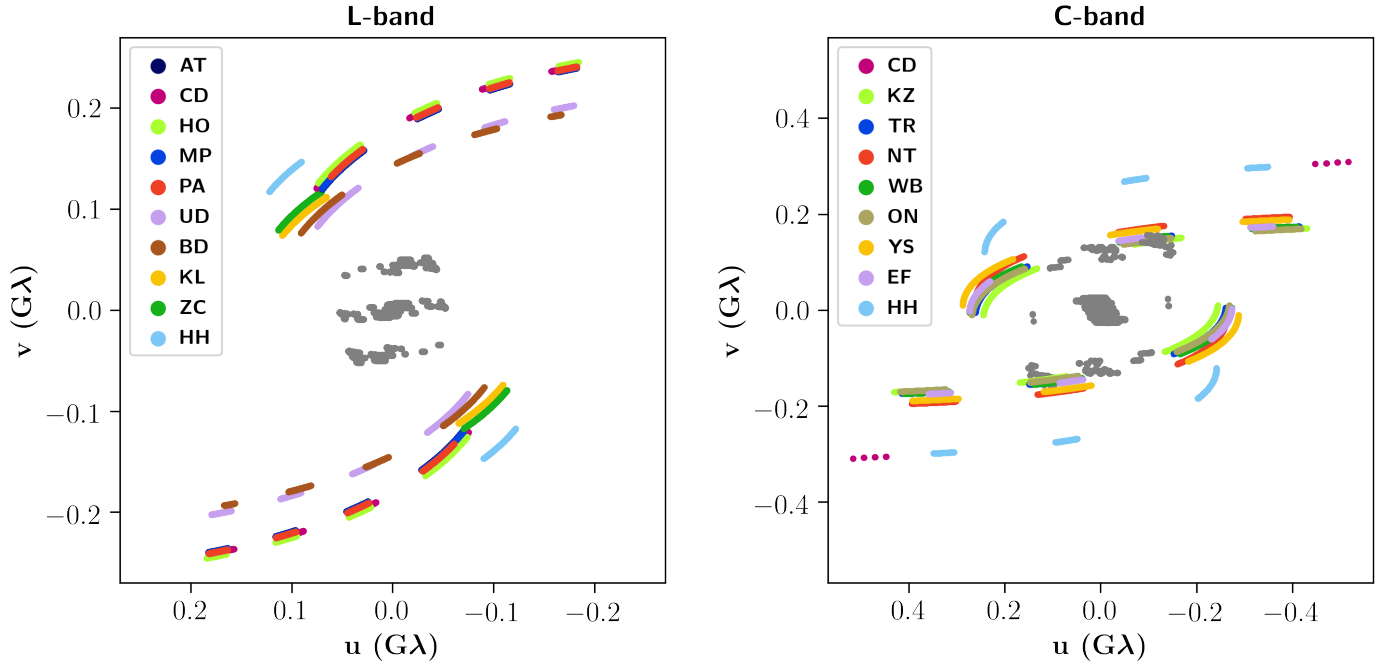


**Fig. 1.**  $u, v$ -coverage for RadioAstron observations at 1.6 GHz (*left panel*) and 4.8 GHz (*right panel*) presented in this work. The central bulge (in grey) of  $u, v$ -tracks span about one Earth diameter (ground stations baselines), while the “wings” (in colors) represent the RadioAstron Space-baselines contribution. Only space-segments giving fringes are plotted, i.e., up to a maximum projected space–ground baseline of  $\sim 4.5$  ED at 1.6 GHz and  $\sim 3.3$  ED at 4.8 GHz.

baselines and a model of the source (baselines stacking within the FRING task in AIPS). This procedure was repeated scan by scan for the SVLBI baselines in order to use a more accurate model describing the source structure. The solution interval was set to 2 min for ground array observations and to 4 min for the SVLBI scans, adopting a signal-to-noise ratio (S/N) threshold of 5. At 1.6 GHz, SVLBI fringes were found on baselines up to  $\sim 4.5$  Earth Diameters (ED), while at 4.8 GHz up to  $\sim 3.3$  ED.

Finally, we imaged the calibrated data in *Di fmap*<sup>2</sup> (Shepherd 1997). First, we flagged RA scans for which SVLBI fringes gave a  $S/N < 5$  in AIPS. Visibilities were then averaged over 30 s at 1.6 GHz, while over 10 s at 4.8 GHz, and the standard uniform weighting scheme ( $uvw = 2, -1$ ) was applied at both frequencies. The source model was built through the standard iterative CLEANing and phase self-calibration technique, adopting solution intervals equal to the data averaging time. The feasibility of phase self-calibration was assured by the high S/N of the visibilities, and the abundance of baselines. Once a satisfactory model was assessed, amplitude self-calibration was performed as well. The shortest amplitude self-calibration solution interval was chosen to be 1 min for both bands. The final images angular resolution and rms were:  $1.04 \times 0.58$  mas and  $3.5$  mJy beam<sup>-1</sup> at 1.6 GHz, while  $0.86 \times 0.46$  mas and  $2.2$  mJy beam<sup>-1</sup> at 4.8 GHz.

### 3. Results

#### 3.1. Limb-brightened jet emission

The RA observations presented in this work allowed us to reach an unprecedented angular resolution at 1.6 GHz for this source, and to detect for the first time a limb-brightened jet in 3C 273 (Fig. 2, left panel). The beam in this image obtained with a uniform weighting scheme is  $1.04 \times 0.58$  mas, with a position angle (PA) of  $79.4^\circ$  and image rms noise of  $3.5$  mJy beam<sup>-1</sup>. As clearly

visible, the structure of the jet is dominated by an elongated structural feature unresolved in the direction orthogonal to the jet for the inner 5 mas from the core, while two distinct emission trails are visible along the rest of the jet, extending towards the south-west for further  $\sim 20$  mas. A brighter region is present at about 15 mas from the core, where the jet bends towards the south, that may be associated with a shock produced by the interaction of the jet with the ambient medium (cf. the cases of 4C 41.17, Gurvits et al. 1997, and J0906+6930, An et al. 2020). This limb-brightened emission was not seen in previous observations of 3C 273, most probably because of the lower angular resolution of previous images (see, e.g., the VLBA image, obtained at 1.7 GHz in 2011, reported in Kovalev et al. 2016).

We further investigated the limb-brightening properties through a detailed tomography along the jet. The MOJAVE team produced stacked images of 373 jets, including 3C 273, at 15 GHz with a time span of 20 years (Pushkarev et al. 2017). As demonstrated in that work, it is necessary to stack the images in order to properly map the full jet width at 15 GHz. In Fig. 3 (right panel), we present the contours from the MOJAVE stacked image overlaid on our *L*-band image, with the purpose of comparing the different structure. A shift of  $43 \times 55$  pixels in RA and Dec, respectively, was applied to align the two images, corresponding to 2.15 mas eastward and 2.75 mas northward (see Sect. 3.2 for a full description of the method). No evident limb-brightened emission is detected in the MOJAVE data. Furthermore, the emission is not symmetric along the full length of the observed jet: the first  $\sim 5$  mas from the core shows an enhanced emission in the southern region, while this shifts to the northern side from  $\sim 5$  to  $\sim 10$  mas. Remarkably, the cores and the innermost  $\sim 5$  mas jet emission are consistent in the two images, and the limb-brightening lies at the edges of the MOJAVE contours. Overall, the MOJAVE intensity distribution, including the jet curvature, is in agreement with our SVLBI results.

<sup>2</sup> <ftp://ftp.astro.caltech.edu/pub/difmap/difmap.html>

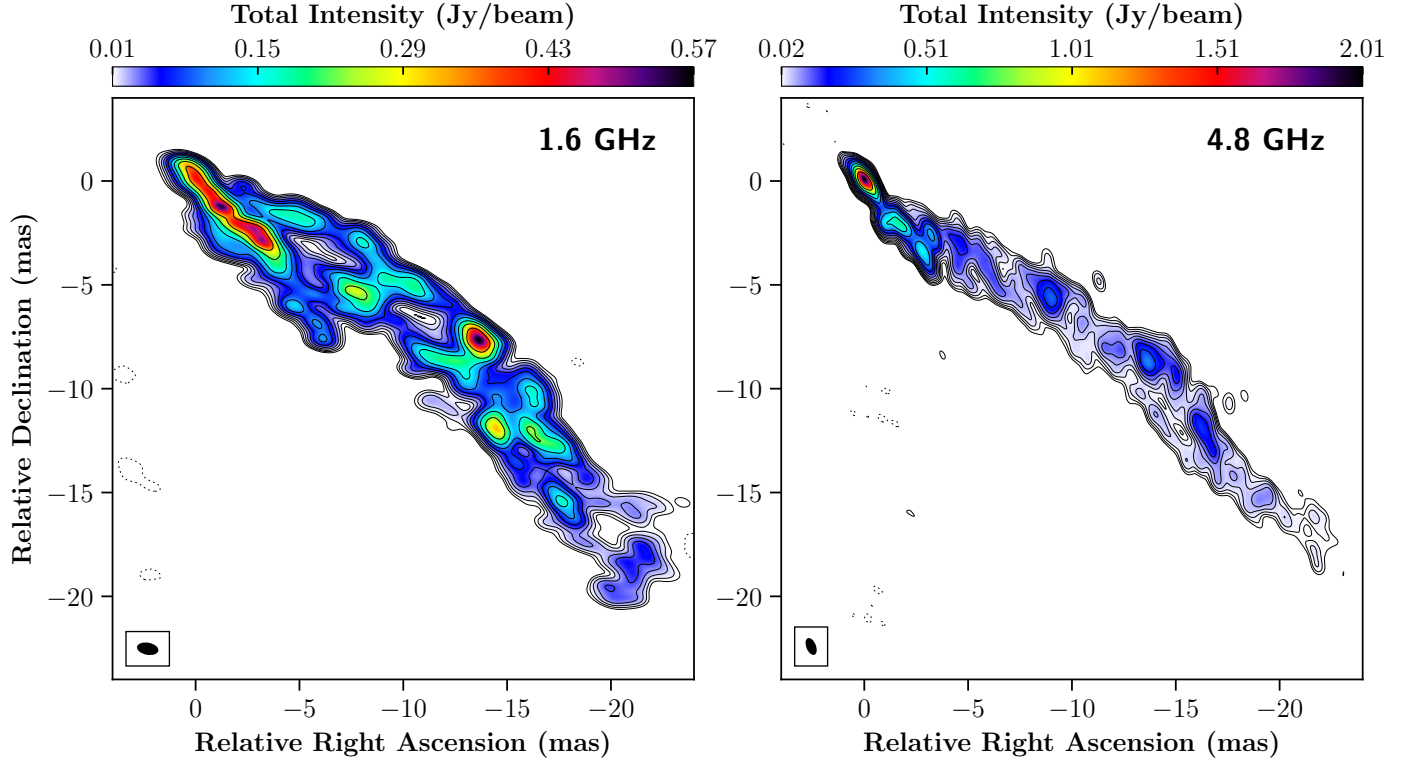


**Fig. 2.** RadioAstron images of 3C 273 at 1.6 GHz (*left panel*, June 2014) and 4.8 GHz (*right panel*, April 2014). The beam is shown on the lower-left corner:  $1.04 \times 0.58$  mas, PA  $79.4^\circ$  at 1.6 GHz, and  $0.86 \times 0.46$  mas, PA  $22.0^\circ$  at 4.8 GHz. The two lowest contour levels are  $\pm 3$  and  $\pm 7$  times the rms of the image noise level ( $3 \times 3.5$  mJy beam $^{-1}$  at 1.6 GHz,  $7 \times 2.2$  mJy beam $^{-1}$  at 4.8 GHz). Successive contours are drawn as  $c_n = (3/2) \times c_{n-1}$  up to 90% of the total intensity peak ( $0.57$  Jy beam $^{-1}$  at 1.6 GHz,  $2.01$  Jy beam $^{-1}$  at 4.8 GHz).

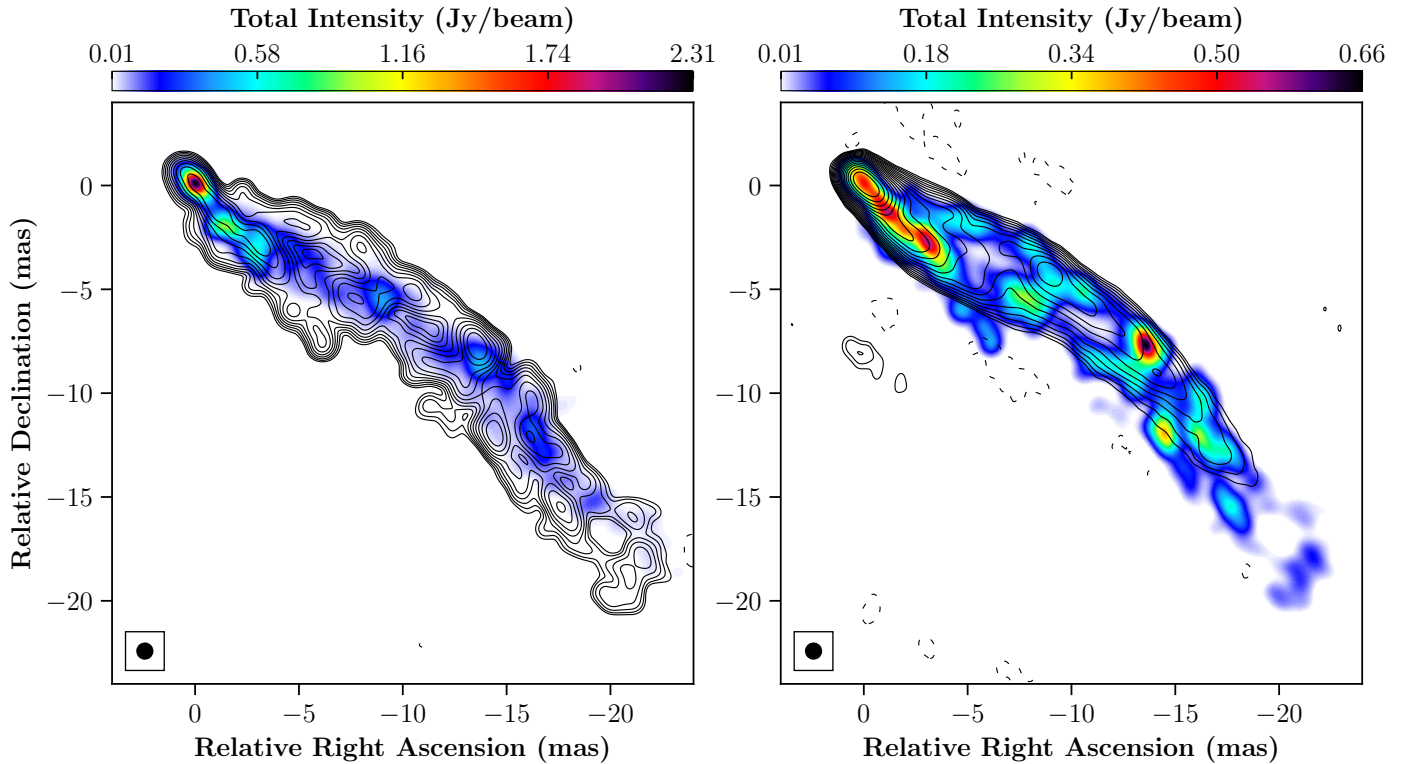


**Fig. 3.** *Left panel:* RadioAstron images of 3C 273 at 1.6 GHz (contours) and 4.8 GHz (in colors) obtained in 2014. Both are convolved with the MOJAVE circular beam ( $0.83 \times 0.83$  mas). *Right panel:* RadioAstron 1.6 GHz image (in colors) with the stacked image from MOJAVE (contours), both convolved with the MOJAVE circular beam of the same size as in the left panel. The two lowest contour levels are  $\pm 5$  and  $\pm 9$  times the rms noise level:  $5 \times 2.8$  mJy beam $^{-1}$  at 1.6 GHz and  $9 \times 0.5$  mJy beam $^{-1}$  at 15 GHz, respectively. Successive contours are drawn as  $c_n = (3/2) \times c_{n-1}$  up to 90% of the total intensity peak ( $0.7$  Jy beam $^{-1}$  at 1.6 GHz,  $6.1$  Jy beam $^{-1}$  at 15 GHz).



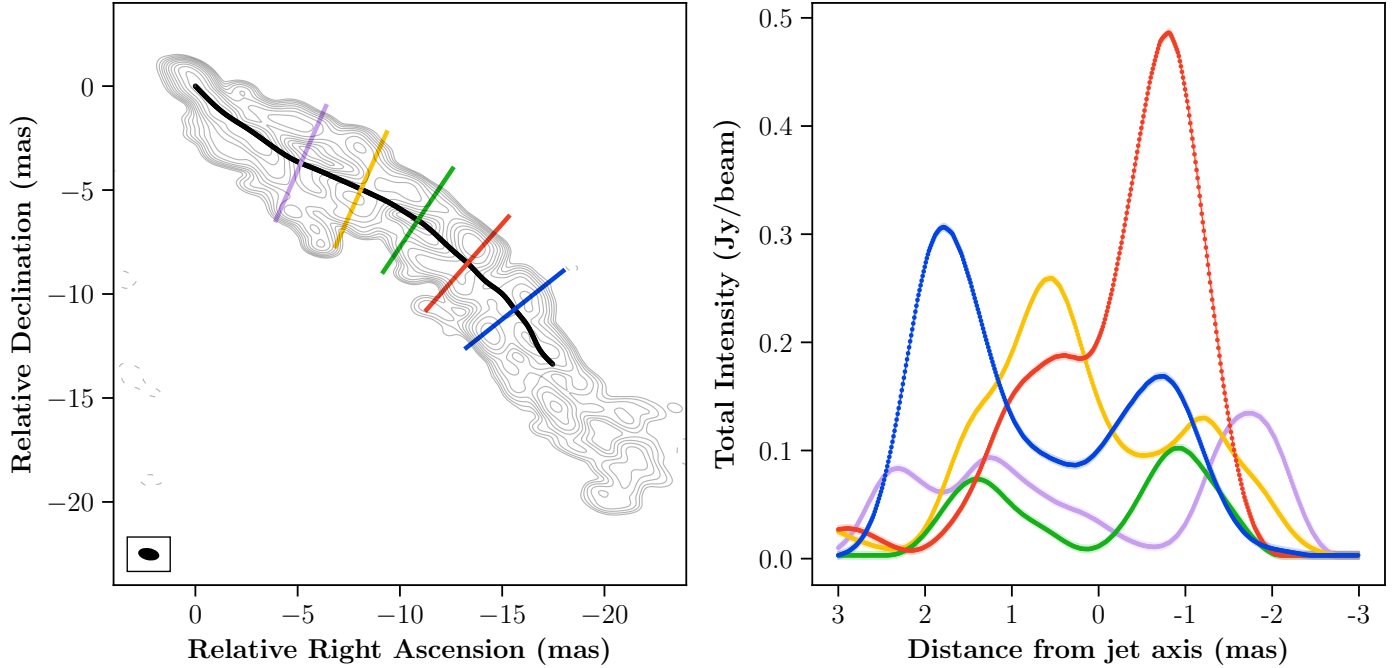


**Fig. 4.** Example of transverse jet brightness profile (*right*) for different positions along the stream axis (*left*) at 1.6 GHz.

We used the jet ridge-line from MOJAVE observations to measure the jet profile along slices perpendicular to it in our RA image, for a total of 440 profiles of 6 mas width. The first 72 profiles, corresponding to the inner 3 mas, do not show a clear double-peaked structure. Down the flow at larger distances, a double structure is visible, but the two peaks are very close to each other. This structure is observed between the inner  $\sim 3$  mas and  $\sim 4$  mas. Beyond 4 mas, the double-peaked structure is more prominent, showing a clear limb-brightening. In Fig. 4, we present five representative jet profiles, clearly showing the double peak resulting from the limbs. The latter can be roughly four times brighter than the central region of the jet. Moreover, as seen in the MOJAVE stacked image, the southern region is brighter in the first few mas from the core, while the northern side is stronger in the second half of the jet.

### 3.2. Evidence of a spine/sheath structure along the jet

Given the results from the 1.6 GHz observations described above, we considered the RA 4.8 GHz image of the same source, obtained less than 2 months earlier, in order to compare the two jet structures. The 4.8 GHz image is presented in Fig. 2: an angular resolution of  $0.86 \times 0.46$  mas was obtained (uniform weighting) with a beam PA of  $22^\circ$ . The average image rms noise is  $\sim 2.2$  mJy beam $^{-1}$ . In this image, a single stream is visible for the whole jet, with no indication of any limb-brightening, contrary to what is seen at 1.6 GHz. Remarkably, the jet curvature is the same as reconstructed in the 1.6 GHz image, and the brighter regions are also in agreement between the two maps.

To better compare the different jet morphologies visible in the two images, we superimposed the 1.6 GHz map with the one at 4.8 GHz, restored with a matched circular beam equal to the MOJAVE one ( $0.83 \times 0.83$  mas). Image registration was performed via a cross-correlation analysis of the total intensity maps (see Gómez et al. 2016, and references therein). In particular, we considered the inner jet spine only, which looks similar in the two images, covering the first  $\sim 5$  mas. Several spectral index maps were produced, adopting a different shift between

the two maps, to identify by visual inspection the one showing the smallest gradients across the jet width (see Plavin et al. 2019 for more details about this method). The final shift adopted was  $36 \times 48$  pixels in RA and Dec, respectively, for the 4.8 GHz image, corresponding to 1.8 mas eastwards and 2.4 mas northwards. The resulting image is presented in Fig. 3 (left panel), where 1.6 GHz is represented in contours and 4.8 GHz in colors. It is evident that the emission at 4.8 GHz falls between the two limbs detected at 1.6 GHz, suggesting that the former traces the jet spine, while the latter the sheath. Although dominance of the jet spine or the jet sheath has been observed in other sources, for the first time here we detect the two structures at frequencies so closely spaced (1.6 GHz vs. 4.8 GHz).

Finally, in order to quantify the prominence of the limbs and the spine at the two frequencies, we traced 300 lines parallel to the jet axis, and calculated the integrated flux density along the lines for both frequencies. To compute the profiles we cut the jet orthogonally to the MOJAVE ridgeline. Since the ridgeline is curved, a line is first fitted between two adjacent points along the ridgeline, then a cut perpendicular to this line is made. We repeat this process for the whole length of the ridgeline and derive the flux density along each cut. Finally, to estimate the profile of the jet flux density between the two sides at 1.6 GHz and 4.8 GHz, we have traced parallel lines to the jet axis (i.e., the MOJAVE ridgeline), also called fluid lines. We created a total of 300 parallel lines, covering the entire jet width, and summed the flux density along the lines. The fluid lines used to integrate the flux density along the flow, with estimated integrated profiles, are shown in Fig. 5. Uncertainties have been computed for each streamline as:

$$\sigma_p = \frac{N}{\sqrt{N_{\text{beams}}}} \sigma_S, \quad (1)$$

where  $N$  and  $N_{\text{beams}}$  are the number of pixels and beams along the streamline, respectively, while  $\sigma_S$  is the standard deviation of the flux density values along it. This formulation, obtained through the covariance matrix calculation, allow us to take into

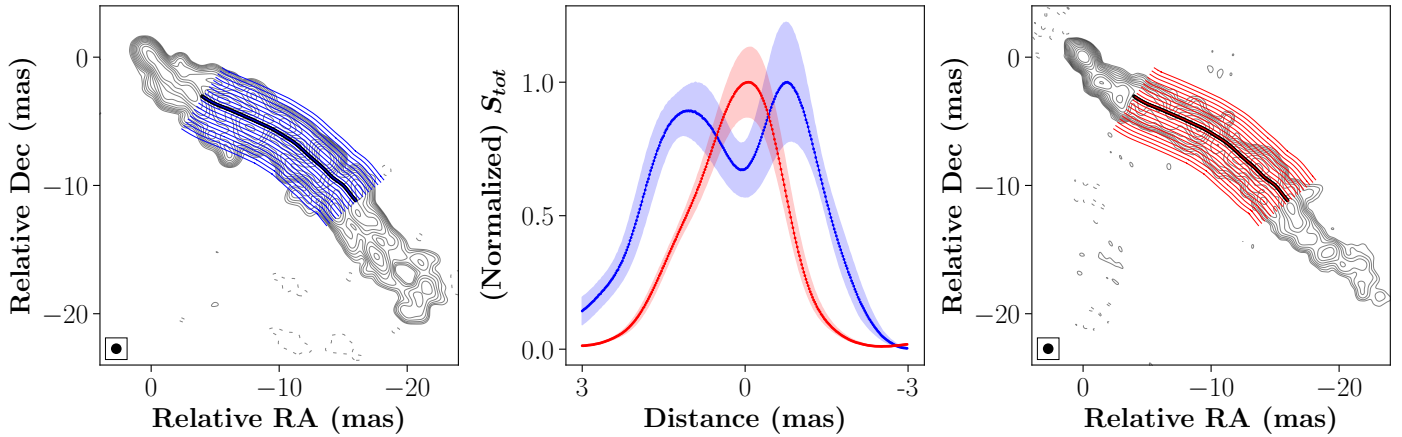


**Fig. 5.** Jet streamlines (300) used to calculate the integrated flux density along the flow, parallel to the jet axis from MOJAVE (central line in black), overplotted on the 1.6 GHz (*left panel*) and 4.8 GHz (*right panel*) RadioAstron contours maps (both convolved with the MOJAVE beam). The starting point is set at 4 mas from the core, where the spine/sheath structure becomes evident. *Central panel*: integrated flux density, versus distance from jet axis, calculated along jet streamlines for the 1.6 GHz (*left*) and 4.8 GHz (*right*) RadioAstron images. The profile uncertainty is reported as a shaded area.

account the correlation of pixels' flux densities within the beam. We found again a tangential double-peaked profile at 1.6 GHz, and a single-peaked one at 4.8 GHz (see Fig. 5), confirming the spine/sheath jet structure.

It should be noted that the double helical structure reported in the C-band image of 3C 273 obtained from the VSOP observation (Lobanov et al. 2000; Lobanov & Zensus 2001) may remain undetected in our C-band image, owing to an  $\approx 3.5$  times smaller beam and a factor of  $\approx 2.5$  lower dynamic range of the RA C-band image presented here. This results in a sensitivity to weak and extended emission almost an order of magnitude lower, which may preclude effective detection of the transverse structure of the flow in the RA image at distances along the jet larger than  $\approx 5$  mas.

## 4. Possible physical factors concurring in the observed jet structure

### 4.1. Propagating structures along the jet

Vega-García (2018) reported an oscillation in the jet direction of 3C 273 between the previous VSOP observation (Lobanov & Zensus 2001) and the RA observation, separated by seventeen years. The author reported an oscillation velocity of  $\approx 0.5c$ , and a pattern speed of  $(0.070 \pm 0.016)c$ . These velocities, clearly smaller than the flow speed revealed by, e.g., the strong brightness asymmetry, show that the observed structures are caused by waves that propagate through the jet (i.e. helical patterns, see Perucho et al. 2012; Cohen et al. 2015; Vega-García et al. 2019). The wavelengths that can be derived from the RA observations reported there coincide with those given in Lobanov & Zensus (2001), plus a further, longer wavelength of  $\approx 50$  mas, due to the sensitivity achieved at larger scales.

In this respect, the limb brightening observed in this work can be caused by a combination of the off-axis pressure enhancements caused by the helical and elliptical waves (see Lobanov & Zensus 2001) and the interaction of the jet with its environment as it oscillates, in the same way as reported by Walker et al. (2018) for the case of M87. The compression of the gas and the magnetic lines due to the medium resistance to jet expansion can cause the observed rise in emissivity.

### 4.2. Velocity stratification in the jet flow

The observed limb-brightening of the RA image at 1.6 GHz requires a stratification across the jet width in the flow density, internal energy, magnetic field, and/or bulk flow velocity. This conclusion is further supported by the 1.6/4.8 GHz spectral index distribution plotted in Fig. 6. This distribution also shows a clear transverse structure in which the spectral index changes between  $-0.2$  and  $+1.7$  along the jet ridge, while it gradually drops below  $-0.7$  towards the jet edges. A stratified jet, with a steep increase in the particle and/or magnetic field energy towards the jet edges can naturally explain the limb brightening and the spectral index distribution, as shown for instance in Ogihara et al. (2019). Transverse stratification of the jet in 3C 273 has indeed been suggested from numerical simulations modelling the Kelvin-Helmholtz instability developing in the flow (Perucho et al. 2006). Numerical simulations also predict a faster jet spine (or beam), surrounded by a slower and denser sheath (see, e.g., the previously mentioned two-fluid models, developed by various authors starting in the 1980s). For a given viewing angle,  $\theta$ , we can compute the Lorentz factor that maximizes the Doppler boosting, which is given by  $\Gamma_{\max} = \sin^{-1} \theta$ . Jets with a bulk Lorentz factor at the jet spine significantly larger than  $\Gamma_{\max}$  will show a limb-brightening, while those with a value similar or smaller than this will show a spine brightening instead.

For 3C 273, several kinematic measurements (Jorstad et al. 2005; Savolainen et al. 2006; Lister et al. 2019) show apparent speeds,  $\beta_{\text{app}}$  in the range of 4–16c, with a median value at around 9c. These measurements support estimates of the viewing angle  $\theta \approx 7^\circ$ – $19^\circ$  and Lorentz factor  $\Gamma \approx 6$ – $16$ . The respective median values of  $\theta = 14^\circ$  and  $\Gamma_b \geq 10$  can be taken as plausible estimates for the spine. The properties of the slower flow can be represented by the Lorentz factor  $\Gamma_s = 2.1 \pm 0.4$  estimated from the analysis of internal structure of the jet emission at 1.6 GHz (Lobanov & Zensus 2001), noting also that the viewing angle estimate of  $15^\circ \pm 3^\circ$  obtained in that analysis agrees well with the median value of the kinematic estimates made for the spine. For these parameters of the spine and flow, the differential Doppler boosting alone should provide limb brightness enhancements by a factor of  $\geq 1.5$ . Hence, the velocity stratification in the jet flow, with a progressive deceleration towards

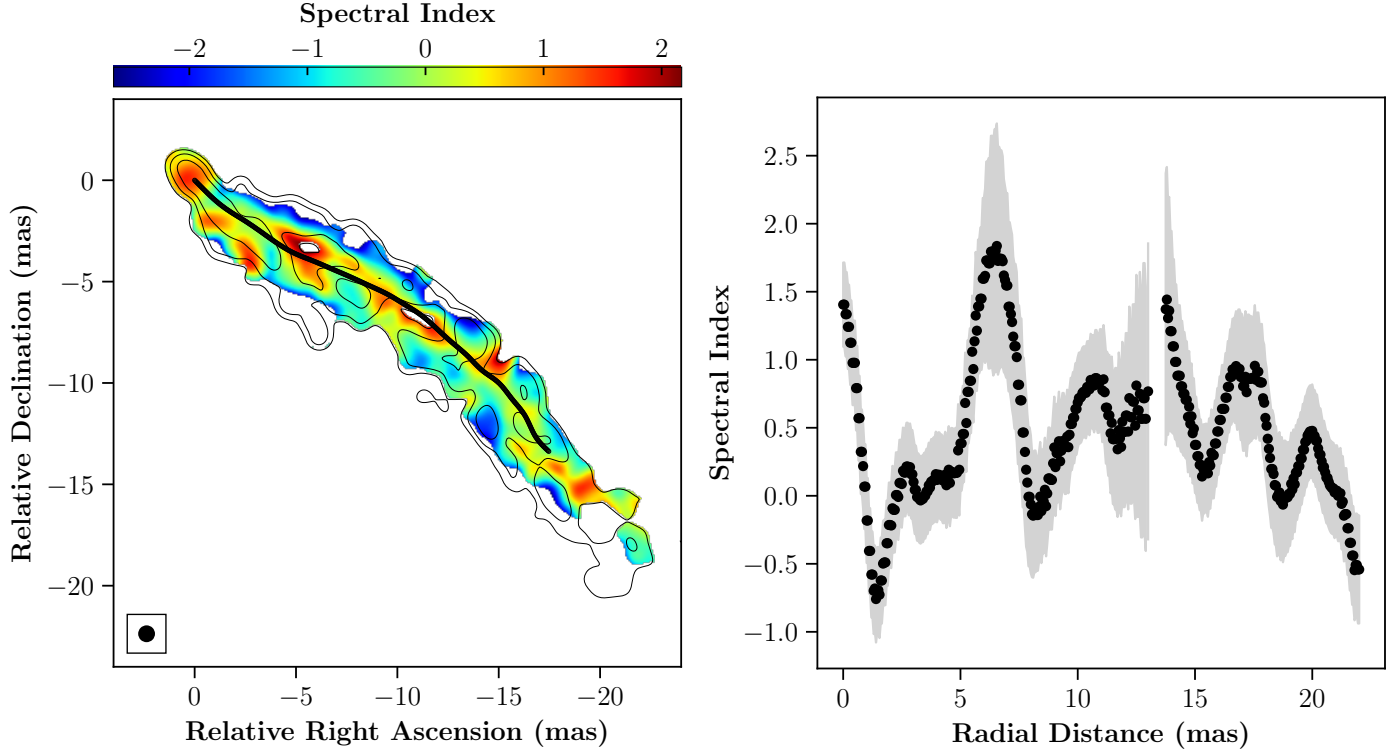


**Fig. 6.** *Left panel:* spectral index map obtained from the RadioAstron images of 3C 273 at 1.6 GHz and 4.8 GHz, both restored considering only the common UV-range 2.5–340  $M\lambda$ , and convolved with the MOJAVE circular beam ( $0.83 \times 0.83$  mas). The map is plotted over the 1.6 GHz image shown in contours. Pixel values below  $5\sigma$  for both the 1.6 GHz and 4.8 GHz images were blanked. *Right panel:* spectral index value and its uncertainty along the jet axis, plotted as a function of the radial distance from the core. The adopted convention for the spectral index  $\alpha$  is  $S \propto \nu^\alpha$ .

the jet edges, may indeed produce the limb-brightening emission seen in the 1.6 GHz RA image.

#### 4.3. Plasma stratification across the jet

Taken alone, the velocity stratification discussed above would equally produce a limb-brightened structure also at 4.8 GHz, which is obviously inconsistent with the observed spine brightening observed at this frequency. For the jet to become spine-brightened at 4.8 GHz, the magnetic field, the density of the emitting plasma, or the electron energy distribution must be varying across the jet. For instance, if higher energy electrons are concentrated around the jet spine, it would cause the emission to become more spine-brightened at progressively higher frequencies. This should lead to a clear stratification in the spectral index across the jet width, as visible in Fig. 6. A similar effect can be achieved by variable opacity across the jet induced by a stratified magnetic field and/or particle density. To provide basic quantitative estimates, we can assume that the flow has a sharp transition from the spine (beam) with the radius  $R_b$  to the sheath with the outer radius  $R_s$ .

Assuming a power-law electron energy distribution  $N(E) = N_0 E^{-s}$  for both these regions, we can write a generic proportionality (Marscher & Gear 1985; Lobanov & Zensus 1999) for the synchrotron flux density received at a frequency  $\nu$  from either of these two regions,  $S_\nu \propto N_0 B^{1-\alpha} V_{\text{em}} \delta^{2-\alpha} \nu^\alpha$ , where  $N_0$  is the particle density,  $B$  is the magnetic field strength,  $V_{\text{em}}$  is the emitting volume,  $\delta$  is the Doppler factor, and  $\alpha$  is the spectral index of the emission. Denoting these quantities with subscripts  $b$  for the spine (beam) and  $s$  for the sheath, we can obtain the ratio  $S_{\nu,b}/S_{\nu,s}$  of the flux densities of the spine and the sheath. From the profiles in the middle panel of Fig. 5, we

estimate  $S_{\nu,b}/S_{\nu,s} \approx 0.7$  and  $R_s \approx 1.9 R_b$ . For an axisymmetric jet structure, the latter translates into the emitting volume ratio  $V_{\text{em},b}/V_{\text{em},s} = R_b^3/(R_s^3 - R_b^3) \approx 0.2$ . The kinematic measurements discussed above yield  $\delta_b \approx 2.8$  and  $\delta_s \approx 3.2$  for the Doppler factors in the spine and the sheath, respectively.

Two scenarios can be considered for the spectral indices of the spine and the sheath. In the first scenario, the spine and the sheath contain plasma with the same electron energy distribution. For this scenario, we set both spectral indices to  $-0.7$ , which corresponds to a commonly assumed  $s = 2.4$  for the electron energy distribution. In the second scenario, the two regions contain different plasmas, and the respective spectral indices also differ. The spectral index image and the ridge line profile of the spectral index in Fig. 6 can be used to estimate  $\alpha_b \approx -0.2$  and  $\alpha_s \approx -0.8$ . The  $\alpha_b$  is estimated from the spectral index of the underlying emission in the spine, while the stretches of higher spectral index observed in that profile must correspond to relativistic shocks propagating through the spine. Indeed, mapping the synchrotron turnover frequency has shown that it is larger than 5 GHz in the shocked regions (Lobanov et al. 1997), and therefore these regions should have a positive 1.6/4.8 GHz spectral index.

With all the estimates discussed above, we obtain for the first scenario  $S_{\nu,b}/S_{\nu,s} \approx 0.07 (N_{0,b}/N_{0,s}) (B_b/B_s)^{1.7}$ . In order to reconcile this relation with the measured flux density ratio of 0.7, the condition  $(N_{0,b}/N_{0,s}) (B_b/B_s)^{1.7} = 9.8$  needs to be satisfied. In stratified jets (Davis & Tchekhovskoy 2020; Komissarov & Porth 2021), the particle density is expected to be lower in the spine, while rising approximately linearly with increasing distance,  $r$ , from the jet axis (Martí et al. 2016) and reaching a maximum inside the sheath or in the transition region. As the onset of the observed transverse stratification occurs at



distances  $\geq 30$  pc from the observed jet origin, the magnetic field there is expected to generate a relatively strong poloidal component (through shear, see [Beuchert et al. 2018](#); [Schulz et al. 2020](#)) dropping off roughly  $\propto r^{-2}$ . In this case, assuming  $N_{0,b} = (R_s/R_b)N_{0,s} = 0.5$  (for linearly increasing particle density), we get  $B_b/B_s \approx 5.6$ . This implies  $B \propto r^{-2.7}$ , which is slightly steeper than the theoretical expectation but can be still viewed as a reasonable agreement. Requiring  $B \propto r^{-2}$  results in  $N \propto r^{0.1}$ , which would imply that both the spine and the sheath are located near the layers of the flow with the maximum particle density.

For the second scenario, with different electron energy distributions in the spine and the sheath, we obtain the ratio  $S_{v,b}/S_{v,s} \approx 0.09 (N_{0,b}/N_{0,s}) (B_b^{1.2}/B_s^{1.8})$ . If one requires that the measured ratio of 0.7 should be explained solely by changes in the electron energy distribution (hence without any stratification in  $N$  and  $B$ ), the latter ratio implies  $B_b = B_s = 30$  mG. At 1 pc distance from the jet origin, the magnetic field strength  $B_{1pc} = 0.3\text{--}1.0$  G has been estimated ([Lisakov et al. 2017](#)). With this estimate and for a poloidally dominated field, one would expect field strengths of  $\approx 4\text{--}10$  mG, averaging to  $B_{avg} \approx 7$  mG, over the region contributing to the transverse profiles plotted in Fig. 5. This is somewhat lower than the field strength of 30 mG needed to explain the measured spine-sheath flux density ratio without stratification of the magnetic field and particle density.

Allowing for the stratification (again, assuming  $N(r) \propto r$  between the spine and the sheath), we get for the magnetic field ratio  $B_b^{1.2}/B_s^{1.8} = 4.3$ . In this case, satisfying the expectation  $B \propto r^{-2}$  for the poloidal field, we get  $B_b = 4.1$  G and  $B_s = 1.1$  G, which are unrealistic for the flow at these distances. Equating  $B_b$  to  $B_{avg} = 7$  mG yields  $B_s = 16$  mG which is difficult to reconcile with the poloidal field. For a toroidally dominated field, estimating the  $B_b$  from  $B_{1pc}$  gives a field strength of  $\approx 70$   $\mu$ G and the respective  $B_s \approx 750$   $\mu$ G. These values both are too low and imply exceedingly steep field gradients across the jet. Altogether, introducing two different electron distributions for the spine and the sheath makes it more difficult to achieve an agreement with the measured flux density ratio. We can therefore conclude that moderately stratified particle density and magnetic field described in the first scenario can be sufficient for explaining the observed limb-brightened jet morphology at 1.6 GHz and spine-brightened structure at 4.8 GHz.

#### 4.4. Potential instrumental effects

Significant gaps in the  $u, v$ -plane can potentially generate artifacts in the final image. The experimental setup of SVLBI observations can easily incur in such issue, when performed with a space antenna at a distance larger than  $\sim 1$  ED from ground. However, depending on the brightness, extension, and morphology of the source under study, the potential artifacts have often a limited impact on the final images. Through a multi-epoch analysis of the jet morphology in S5 0836+710, [Perucho et al. \(2012\)](#) and [Vega-García et al. \(2019\)](#) discussed how  $u, v$ -coverage should not introduce relevant differences on the observed jet structure, but only minor ripples along the ridge lines. Indeed, they found the latter to be consistent among different epochs of observations, and instrumental setups. The features discussed in the present work are prominent ( $S/N > 100$ ), with an extension of several beams, and visible as long waves along the jet ( $\sim 10$  mas), so we can reasonably exclude an instrumental effect due to gaps in  $u, v$ -coverage. In addition, it has been shown that spectral indices (and then flux distribution) obtained from observations with uneven  $u, v$ -coverage can be trusted (i.e. have an accuracy  $> 90\%$ ) for a sufficient pixel  $S/N$  ( $> 5$ ), and when

within 10–15 mas from the phase-center ([Lobanov 1998](#)). Both those conditions are satisfied by the structures presented in this work.

## 5. Conclusions

We have presented an analysis of RA images at 1.6 GHz and 4.8 GHz for 3C 273, the former being the highest angular resolution image to date for this source at this frequency. Our findings can be summarized as follows:

- For the first time, a limb-brightened emission is evident in the image at 1.6 GHz, showing an enhanced emission for the two edges of the jet, starting from about 4 mas from the core and following the whole jet extension.
- Conversely, at 4.8 GHz only a single stream is detected, consistently located between the edges of the 1.6 GHz jet. This is confirmed by the jet profile drawn from the integrated flux density along the jet streamlines, indicating a double-peaked profile at 1.6 GHz and a single-peaked one at 4.8 GHz.
- The observed morphology is indicative of a spine/sheath structure in the jet. This can be explained in terms of the following, concurring, physical factors: (1) helical patterns propagating along the jet, similar to the ones reported in previous Space-VLBI observations of this source ([Lobanov & Zensus 2001](#)); (2) a velocity stratification in the jet flow, with a faster jet spine and a slower and denser sheath; (3) plasma stratification across the jet, necessary to produce the noticeable morphological differences between the two observed close frequencies. This stratification scenario is supported by the spectral index gradient measured across the jet, and consistent along its extension.

A more detailed quantitative consideration through dedicated general relativistic magneto-hydrodynamical numerical simulations, able to reproduce the spine/sheath structure seen in these RA observations of 3C 273, will be published in a future work.

**Acknowledgements.** We thank the anonymous referee for useful comments. JLG and AF acknowledge financial support from the Spanish Ministerio de Economía y Competitividad (grants AYA2016-80889-P, PID2019-108995GB-C21), the Consejería de Economía, Conocimiento, Empresas y Universidad of the Junta de Andalucía (grant P18-FR-1769), the Consejo Superior de Investigaciones Científicas (grant 2019AEP112), and the State Agency for Research of the Spanish MCIU through the Center of Excellence Severo Ochoa award for the Instituto de Astrofísica de Andalucía (SEV-2017-0709). APL, YYK, and ABP were supported by the Russian Science Foundation (project 20-62-46021). TS was partly supported by the Academy of Finland projects 274477 and 315721. MP acknowledges the support by the Spanish Ministerio de Ciencia e Innovación (MICINN) under grant PID2019-105510GB-C31. MP and JMM acknowledge financial support from the Spanish Ministry of Science through Grants PID2019-107427GB-C33 and AYA2016-77237-C3-3-P, and from the Generalitat Valenciana through grant PROMETEU/2019/071. JMA was supported by the German Research Foundation grant HE5937/2-2. LIG acknowledges support by the CSIRO Distinguished Visitor Programme. The RadioAstron project is led by the Astro Space Center of the Lebedev Physical Institute of the Russian Academy of Sciences and the Lavochkin Scientific and Production Association under a contract with the Roscosmos State Corporation, in collaboration with partner organizations in Russia and other countries. This publication has received funding from the European Union's Horizon 2020 research and innovation programme under grant agreement No. 730562 [RadioNet]. This paper includes data observed with the 100-m Effelsberg radio-telescope, which is operated by the Max-Planck-Institut für Radioastronomie in Bonn (Germany). The National Radio Astronomy Observatory is a facility of the National Science Foundation operated under cooperative agreement by Associated Universities, Inc. The European VLBI Network is a joint facility of independent European, African, Asian, and North American radio astronomy institutes. The Long Baseline Array is part of the Australia Telescope National Facility which is funded by the Australian Government for operation as a National Facility managed by CSIRO. This research made use of Python (<http://www.python.org>), Numpy ([van der Walt et al. 2011](#)), Pandas ([McKinney 2010](#)), and Matplotlib ([Hunter 2007](#)). We also made use of Astropy



(<http://www.astropy.org>), a community-developed core Python package for Astronomy (Astropy Collaboration 2013, 2018).

## References

- An, T., Mohan, P., Zhang, Y., et al. 2020, *Nat. Commun.*, **11**, 143
- Asada, K., & Nakamura, M. 2012, *ApJ*, **745**, L28
- Astropy Collaboration (Robitaille, T. P., et al.) 2013, *A&A*, **558**, A33
- Astropy Collaboration (Price-Whelan, A. M., et al.) 2018, *AJ*, **156**, 123
- Attridge, J. M., Roberts, D. H., & Wardle, J. F. C. 1999, *ApJ*, **518**, L87
- Beuchert, T., Kadler, M., Perucho, M., et al. 2018, *A&A*, **610**, A32
- Blandford, R. D., & Payne, D. G. 1982, *MNRAS*, **199**, 883
- Blandford, R. D., & Znajek, R. L. 1977, *MNRAS*, **179**, 433
- Boccardi, B., Krichbaum, T. P., Bach, U., Bremer, M., & Zensus, J. A. 2016, *A&A*, **588**, L9
- Bruni, G., Anderson, J., Alef, W., et al. 2016, *Galaxies*, **4**, 55
- Bruni, G., Gómez, J. L., Casadio, C., et al. 2017, *A&A*, **604**, A111
- Bruni, G., Savolainen, T., Gómez, J. L., et al. 2020, *Adv. Space Res.*, **65**, 712
- Celotti, A., Ghisellini, G., & Chiaberge, M. 2001, *MNRAS*, **321**, L1
- Cohen, M. H., Meier, D. L., Arshakian, T. G., et al. 2015, *ApJ*, **803**, 3
- D’Arcangelo, F. D., Marscher, A. P., Jorstad, S. G., et al. 2009, *ApJ*, **697**, 985
- Davis, S. W., & Tchekhovskoy, A. 2020, *ARA&A*, **58**, 407
- Ghisellini, G., Tavecchio, F., & Chiaberge, M. 2005, *A&A*, **432**, 401
- Giovannini, G., Savolainen, T., Orienti, M., et al. 2018, *Nat. Astron.*, **2**, 472
- Giroletti, M., Giovannini, G., Feretti, L., et al. 2004, *ApJ*, **600**, 127
- Gómez, J. L., Lobanov, A. P., Bruni, G., et al. 2016, *ApJ*, **817**, 96
- Gurvits, L. I., Schilizzi, R. T., Miley, G. K., et al. 1997, *A&A*, **318**, 11
- Hardee, P. E. 2007, *ApJ*, **664**, 26
- Hazard, C., Mackey, M. B., & Shimmins, A. J. 1963, *Nature*, **197**, 1037
- Hunter, J. D. 2007, *Comput. Sci. Eng.*, **9**, 90
- Johnson, M. D., Kovalev, Y. Y., Gwinn, C. R., et al. 2016, *ApJ*, **820**, L10
- Jorstad, S. G., Marscher, A. P., Lister, M. L., et al. 2005, *AJ*, **130**, 1418
- Kardashev, N. S., Khartov, V. V., Abramov, V. V., et al. 2013, *Astron. Rep.*, **57**, 153
- Kim, J. Y., Krichbaum, T. P., Lu, R. S., et al. 2018, *A&A*, **616**, A188
- Komissarov, S., & Porth, O. 2021, *New Astron. Rev.*, **92**, 101610
- Kovalev, Y. Y., Kardashev, N. S., Kellermann, K. I., et al. 2016, *ApJ*, **820**, L9
- Kovalev, Y. Y., Pushkarev, A. B., Nokhrina, E. E., et al. 2020a, *MNRAS*, **495**, 3576
- Kovalev, Y. Y., Kardashev, N. S., Sokolovsky, K. V., et al. 2020b, *Adv. Space Res.*, **65**, 705
- Lisakov, M. M., Kovalev, Y. Y., Savolainen, T., Hovatta, T., & Kutkin, A. M. 2017, *MNRAS*, **468**, 4478
- Lister, M. L., Homan, D. C., Hovatta, T., et al. 2019, *ApJ*, **874**, 43
- Lobanov, A. P. 1998, *A&AS*, **132**, 261
- Lobanov, A. P., & Zensus, J. A. 1999, *ApJ*, **521**, 509
- Lobanov, A. P., & Zensus, J. A. 2001, *Science*, **294**, 128
- Lobanov, A. P., Carrara, E., & Zensus, J. A. 1997, *Vistas Astron.*, **41**, 253
- Lobanov, A. P., Zensus, J. A., Abraham, Z., et al. 2000, *Adv. Space Res.*, **26**, 669
- Marscher, A. P., & Gear, W. K. 1985, *ApJ*, **298**, 114
- Martí, J. M., Perucho, M., & Gómez, J. L. 2016, *ApJ*, **831**, 163
- McKinney, W. 2010, in *Proceedings of the 9th Python in Science Conference*, eds. S. van der Walt, & J. Millman, 51
- Mertens, F., Lobanov, A. P., Walker, R. C., & Hardee, P. E. 2016, *A&A*, **595**, A54
- Mimica, P., Giannios, D., Metzger, B. D., & Aloy, M. A. 2015, *MNRAS*, **450**, 2824
- Nokhrina, E. E., Kovalev, Y. Y., & Pushkarev, A. B. 2020, *MNRAS*, **498**, 2532
- Ogihara, T., Takahashi, K., & Toma, K. 2019, *ApJ*, **877**, 19
- Oke, J. B. 1963, *Nature*, **197**, 1040
- Pelletier, G., & Roland, J. 1989, *A&A*, **224**, 24
- Perucho, M., Lobanov, A. P., Martí, J. M., & Hardee, P. E. 2006, *A&A*, **456**, 493
- Perucho, M., Kovalev, Y. Y., Lobanov, A. P., Hardee, P. E., & Agudo, I. 2012, *ApJ*, **749**, 55
- Plavin, A. V., Kovalev, Y. Y., Pushkarev, A. B., & Lobanov, A. P. 2019, *MNRAS*, **485**, 1822
- Pushkarev, A. B., Gabuzda, D. C., Vetukhnovskaya, Y. N., & Yakimov, V. E. 2005, *MNRAS*, **356**, 859
- Pushkarev, A. B., Kovalev, Y. Y., Lister, M. L., & Savolainen, T. 2017, *MNRAS*, **468**, 4992
- Savolainen, T., Wiik, K., Valtaoja, E., & Tornikoski, M. 2006, *A&A*, **446**, 71
- Schmidt, M. 1963, *Nature*, **197**, 1040
- Schulz, R., Kadler, M., Ros, E., et al. 2020, *A&A*, **644**, A85
- Shepherd, M. C. 1997, in *Astronomical Data Analysis Software and Systems VI*, eds. G. Hunt, & H. Payne, *ASP Conf. Ser.*, **125**, 77
- Sikora, M., Stawarz, L., & Lasota, J.-P. 2007, *ApJ*, **658**, 815
- Sol, H., Pelletier, G., & Asseo, E. 1989, *MNRAS*, **237**, 411
- Tavecchio, F., & Ghisellini, G. 2008, *MNRAS*, **386**, 945
- van der Walt, S., Colbert, S. C., & Varoquaux, G. 2011, *Comput. Sci. Eng.*, **13**, 22
- Vega-García, L. 2018, PhD Thesis, Universität zu Köln, Germany
- Vega-García, L., Perucho, M., & Lobanov, A. P. 2019, *A&A*, **627**, A79
- Walker, R. C., Hardee, P. E., Davies, F. B., Ly, C., & Junor, W. 2018, *ApJ*, **855**, 128
- Xie, W., Lei, W.-H., Zou, Y.-C., et al. 2012, *Res. Astron. Astrophys.*, **12**, 817